Deformable 2D-3D Registration of Vascular Structures in a One View Scenario

Martin Groher*, Darko Zikic, and Nassir Navab

***Abstract*—Alignment of angiographic 3D scans to 2D projections is an important issue for 3D depth perception and navigation during interventions. Currently, in a setting where only one 2D projection is available, methods employing a rigid transformation model present the state of the art for this problem. In this work, we introduce a method capable of deformably registering 3D vessel structures to a respective single projection of the scene. Our approach addresses the inherent ill-posedness of the problem by incorporating *a priori* knowledge about the vessel structures into the formulation. We minimize the distance between the 2D points and corresponding projected 3D points together with regularization terms encoding the properties of length preservation of vessel structures and smoothness of deformation. We demonstrate the performance and accuracy of the proposed method by quantitative tests on synthetic examples as well as real angiographic scenes.**

***Index Terms*—Angiography, deformable registration, 2D-3D registration.**

I. Introduction

ANGIOGRAPHIC imaging is a widely used technique for visualization of vessel anatomy in diagnosis and treatment. During most abdominal catheterizations, contrasted 2D projections from one view are acquired by a C-arm for catheter guidance and treatment monitoring. A 3D angiographic scan[1] is usually acquired preoperatively to assess the region of interest and identify possible complications for the treatment. This 2D/3D setting is sketched in Fig. 1. In clinical practice, the available 3D information is currently not brought to the interventional room. In some interventions, 3D intraoperative data is available from rotational angiography. This data set, however, is currently not used for guidance or navigation, where 2D projections are favored since they capture the temporal changes compared to a static 3D scan. Only guided by images from one view, it is often very difficult for the physician to find a path through the patient's vessel system. This is mainly due to overlap of vessel structures and breathing deformation.

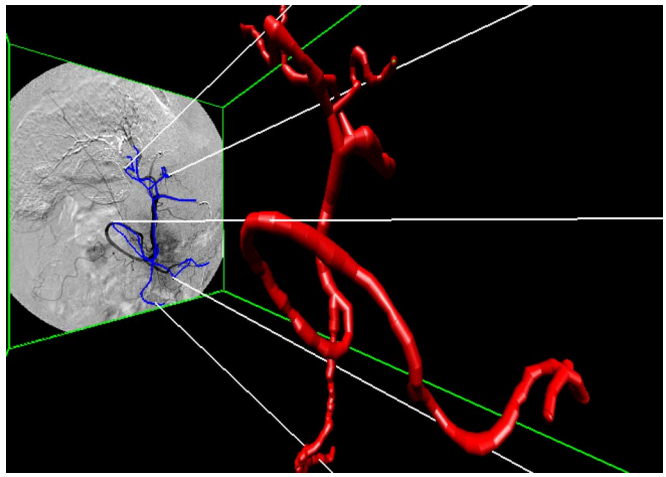

Fig. 1. Visualization of the 2D/3–D C-arm/patient scenario. The 3D vasculature is to be deformably registered to the 2D projection image. The blue line in the 2D digitally subtracted angiogram (DSA) visualizes the projected centerline of the rigidly registered 3–D vasculature. This projection is visibly deformed to the projection in the DSA due to breathing motion.

An accurate registration of 3D to 2D vasculature would allow for intraoperative 3D roadmapping or catheter tip backprojection. With this 3D enhancement of angiographic interventions, an increase in depth perception can be achieved while the amount of injected contrast agent and radiation dose can be reduced.

In abdominal or thoracic regions that are subject to deformation, this registration cannot be established by a mere rigid or affine transformation model (for an example, see Fig. 9). Instead, it is necessary to create a 3D deformation field that locally deforms the 3D vasculature such that its projection matches the 2D vasculature.

For 3D-3D registration of vascular images, methods have been developed to compute the deformation field from sparse correspondences that are determined manually or through rigid prealignment [1], [2]. However, the computation of a dense 3D deformation field from sparse 2D-3D feature correspondences is in general an ill-posed problem. The displacement of a point along the projection ray cannot be computed without additional constraints, compare Figs. 2 and 3.

Currently, methods for 2D-3D alignment of vascular images use a rigid transformation model discarding local motion. Such algorithms tend to be robust against deformation changes of vessel structures but do not solve for these deformations, leaving a considerable amount of misalignment, which can be, as reported for e.g., liver, up to 3 cm [3].

Manuscript received September 07, 2008; revised November 13, 2008. First published January 06, 2009; current version published May 28, 2009. This work was supported in part by an academic grant from Siemens Healthcare, Angiography/X-Ray division, Forchheim, Germany and in part by Siemens Corporate Research, Princeton, NJ. *Asterisk indicates corresponding author.*

*M. Groher is with the Chair for Computer Aided Medical Procedures and Augmented Reality, Technische Universität München, 85748 Munich, Germany (e-mail: groher@cs.tum.edu).

D. Zikic and N. Navab are with the Chair for Computer Aided Medical Procedures and Augmented Reality, Technische Universität München, 85748 Munich, Germany (e-mail: zikic@cs.tum.edu; navab@cs.tum.edu).

Color versions of one or more of the figures in this paper are available online at http://ieeexplore.ieee.org.

Digital Object Identifier 10.1109/TMI.2008.2011519

[1]Computed Tomography Angiography (CTA), Magnetic Resonance Angiography (MRA).

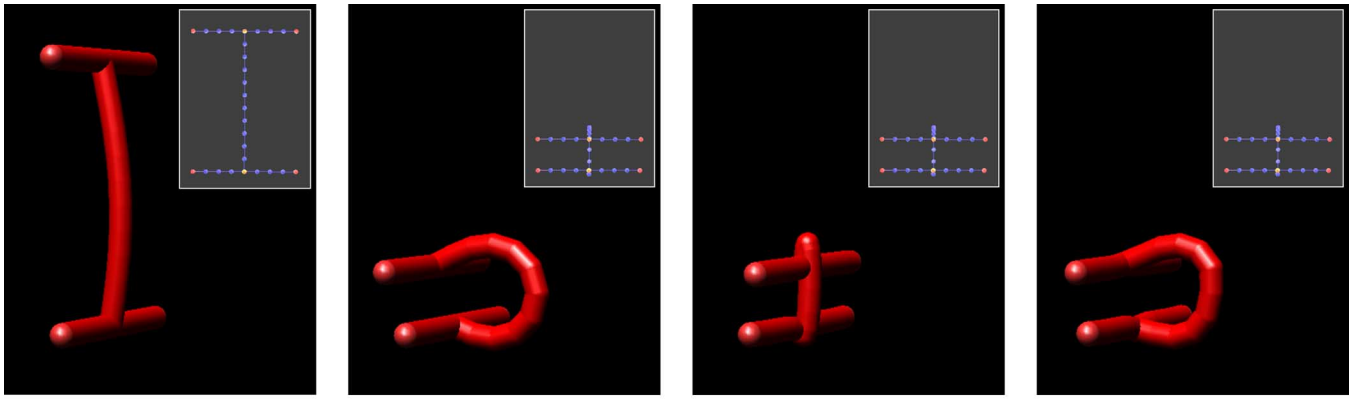

Fig. 2. Visualization of the method results on a simple synthetic example, with the window-in-window presenting the 2D projection of the respective 3D structure. (a) Is the input 3D vessel graph to be deformed while (b) shows a vessel graph, which was used to generate the input 2D projection image. Hence, (b) presents the ground truth for the deformation of (a). The camera is positioned on the right side of the images, such that the shape change in ray direction is not observable from the 2D projection image. (c) With the naïve approach using only the distance measure from a single projection, it is not possible to recover the full 3D deformation since there are no constraints along the projection rays. (d) Employing the length preservation and diffusion regularization terms present additional constraints and thus allows for correct deformation also in the direction along the projection rays.

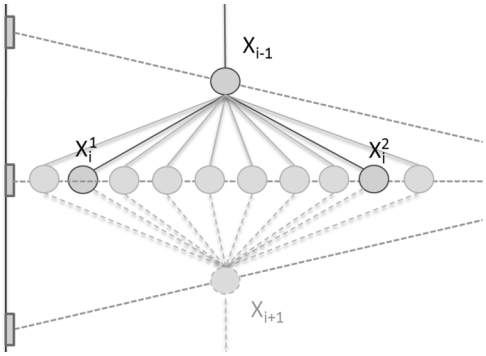

Fig. 3. Illustrates the reduction of admissible solutions for one node along the projection ray, by using length preservation. For the fixed node $\mathbf{X}_{i-1}$, the position of the node $\mathbf{X}_i$ is constrained to two possible solutions, $\mathbf{X}_i^1$ and $\mathbf{X}_i^2$, if the distance between $\mathbf{X}_{i-1}$ and $\mathbf{X}_i$ is assumed constant. Without the length constraint, every position along the ray presents a solution, some of which are visualized above.

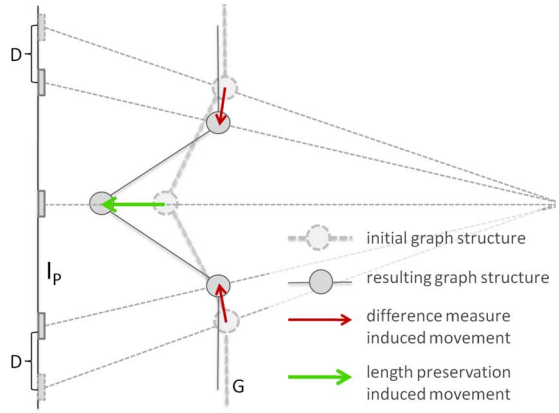

Fig. 4. 2D illustration of the effect of the difference measure and the length preservation term on the motion of the vessel structure. The difference term D measures the distance in the 2D projection image I_p. The length preservation penalizes the change of length of the 3D graph G.

In order to overcome the shortcomings of the rigid approach, we propose a method for computing a meaningful deformation of a 3D structure from a single 2D projection. Our method combines the correspondence-based approach and the ideas from intensity-based registration, where the registration problem is defined as a minimization of an energy consisting of a difference measure and regularization terms, which incorporate the *a priori* knowledge about the problem, see Fig. 2.

The difference term used in our approach penalizes the distance between the projection of 3D points from the input vasculature, represented as nodes of a centerline graph, and the corresponding points from the 2D projection image (Fig. 4).

Minimizing only the difference term results in what we refer to as the *Naïve approach*, which is not able of recovering the deformation in the projection direction and thus can lead to unnatural results. In order to be able to compute the 3D displacement, additionally to the difference, we employ a combination of two regularization terms, which model assumptions about vessel structures and thus yield more realistic deformations.

The first term describes the assumption that the length of vessels does not change heavily inside the human body and penalizes large changes of the vessel length. This term is important since it presents constraints in 3D space and thus reduces the number of solutions for one node from infinitely many to two solutions along the projection ray, if one of the neighbors is assumed fixed (Fig. 3). Also, in our experiments the minimization of this term by steepest gradient descent results in the nearest solution to the initial position of the respective point. Fig. 4 illustrates the idea of using the difference term together with length preservation.

However, graphs that are extracted from real vessel structures can have many nodes and large deformations. Here, the length preservation term has the drawback that the behavior is too local. Although the length preservation itself is performed successfully, in these cases the property that the nearest solution to the initial position is computed introduces unnatural bends in the vessels, thus leading to unwanted results, compare Fig. 5. In

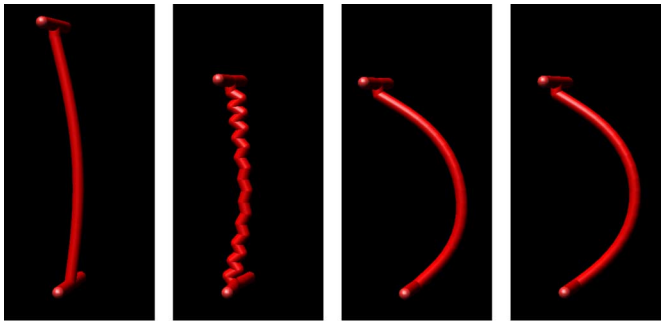

Fig. 5. Demonstrates the effect of joint usage of the length preservation and the diffusion regularization term. (a) Input 3D image. (b) Result with length preservation. (c) Result with length preservation and diffusion regularization clearly produces a more natural result. (d) Ground truth.

order to counteract this effect, we impose a smoothness condition on the resulting displacement field. To this end, we employ the Diffusion regularization term [4], which is often used in intensity-based image registration.

So in summary, our method enables meaningful 3D deformations of 3D vessel structures based on a single 2D projection of the same structure. To the best of our knowledge this is the first time that this problem is addressed in the field of medical image processing.

A. Relation to Prior Work

There is a considerable body of research on *rigid* 2D-3D registration of vascular images, which however mostly addresses rigid structures, for example in neurosurgery, see [5]–[13]. For the case of abdominal or thoracic 2D-3D image alignment, there exist some methods, which are supplemented by gating information or robustness against deformations [14]–[17]. However, although robust to local transformations, these methods still use a rigid transformation model and do not account for the occurring deformation.

Within the context of registration of two or more 2D projections to an atlas or statistical model of bone anatomy, 2D-3D deformable registration has been addressed by Fleute *et al.* [18], Benameur *et al.* [19], Yao *et al.* [20], Zheng *et al.* [21], and Tang *et al.* [22]. These methods do not focus on vessel anatomy and do not cope with a single view scenario.

Regarding the usage of the constraint of length preservation of vessel structures for image registration, to our knowledge, there is no previous work in the literature.

In the robotics and graphics community, computing the 3D pose of a model from a 2D image is regarded as an inverse kinematics problem (see e.g., Grochow *et al.* [23] and references therein), which is somewhat related to our topic. However, the model which is used in these approaches often just has a very limited number of degrees-of-freedom (DOF) unlike our model, where each feature point introduces 3 DOF.

II. Method

The basic idea of the proposed method is to use a difference term and supplement it by regularization terms which incorporate *a priori* knowledge about the problem and thus impose constraints along the projection rays, which are needed in order to render the problem well posed.

Having modeled the problem this way, the solution is computed by using an optimization method of choice.

In Section II-A, we first briefly describe the setting for the algorithm and the performed preprocessing steps. We go on by presenting notation and introducing structures we use in Section II-B. Section II-C will introduce our core model, which is split into difference term (Section II-D), length preservation (Section II-E), and regularization (Section II-F). An algorithmic summary of our model is given in II-G. For a better understanding of the model, we assume correspondence information to be given in Sections II-C–II-G. In Section II-H we extend our algorithm by an iterative assignment of correspondences using a closest-point criteria. We summarize the overall algorithm in Section II-I before experimental setups and results are presented in Section III.

A. Setting and Preprocessing

As input for our method we use an extracted model of 2D and 3D vasculature, as well as a feature-based rigid prealignment in a calibrated setting[2] yielding a projection matrix. All of these steps have been previously presented in the literature and are not within the scope of this paper. A graph model is created in both 2D and 3D from a region growing step yielding vessel segmentations, followed by topological thinning and bifurcation detection as described in [24] and [25]. A rigid 2D-3D registration is computed by distance minimization of 2D and projected 3D centerline curves as has been successfully applied to vessels (see e.g., [6], [15]) solving for a projection matrix. 2D and 3D vessel systems are rather different due to local and global contrast injection protocols and segmentation errors. Thus, assigning point correspondences is not straight forward even if a projection matrix is known. In the first sections (Sections II-C–II-G), however, we assume corresponding information to be given. In Section II-H, we incorporate the computation of 2D-3D correspondences into our algorithm by iteratively updating an *assignment matrix*, which stores correspondence probabilities of 3D and 2D points as well as outlier information.

B. Preliminaries and Notation

We model vessel structures as directed graphs $G^d = (V^d, E^d)$, with a set of n nodes $V^d \subset \mathbb{R}^d$ and the connecting edges $E^d \subset V^d \times V^d$. Here $d \in \{2, 3\}$ denotes the dimension of the graph. For the following, refer also to Fig. 6.

The nodes are classified either as bifurcation nodes V_b^d or sampling nodes V_s^d, such that $V^d = V_b^d \cup V_s^d$ and $\emptyset = V_b^d \cap V_s^d$. While the bifurcation nodes express the topology and the rough geometry of the vessel tree, the sampling nodes are used to describe the geometry of the vessel segments in more detail.

The bifurcation nodes are abbreviated by $\mathbf{B}$ and are identified with their spatial coordinates, such that $\mathbf{B} \in V^d$.

We denote the sampling nodes by $\mathbf{X}$ in 3D and $\mathbf{x}$ in 2D and again identify them with their spatial coordinates.

[2]Meaning that intrinsic parameters of the intraoperative imaging device are given. Also, image distortion can be assumed to be absent due to flat-panel detector technology.

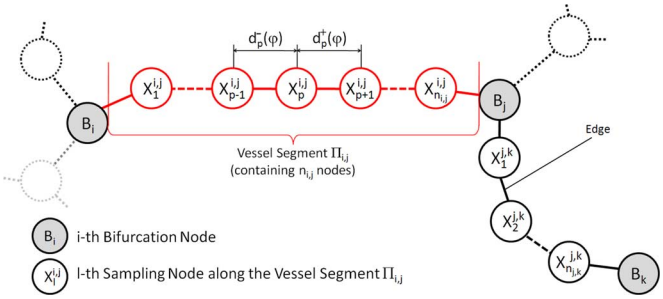

Fig. 6. Illustration of the used graph structure.

The correspondences between the 3D and 2D points are represented by $C \subset V^3 \times V^2$.

We define a vessel segment $\Pi_{i,j}$ as a path between two neighboring bifurcation nodes $\mathbf{B}_i$ and $\mathbf{B}_j$, containing all sampling nodes and edges between $\mathbf{B}_i$ and $\mathbf{B}_j$. The number of nodes in $\Pi_{i,j}$ is $n_{i,j}$ and the number of edges is, respectively, $n_{i,j}+1$. The sampling nodes are indexed relative to the vessel segment $\Pi_{i,j}$ starting from 1 to $n_{i,j}$, compare Fig. 6.

The deformation function is encoded by a set of 3D displacement vectors $\varphi \in \mathbb{R}^{3\times n}$ centered in the n corresponding graph nodes. The displacement at the ith node $\mathbf{X}_i$ is denoted by φ_i, such that the final position of the node is $\mathbf{Y}_i = \mathbf{X}_i + \varphi_i$.

We also employ a dense version of the displacement function, which we denote by φ_{TPS}. We obtain φ_{TPS} from φ by interpolation using thin-plate splines (TPSs) [26]. Interpolating as well as approximating TPS have been successfully applied in deformable registration of medical images, see for instance [27], [28], the latter one being a good introductory reference. In our work we merely use the TPS as an interpolation scheme, i.e., to create a dense displacement field for assigning displacement values to nodes for which no displacement vectors are defined.[3]

For projections we use a standard pinhole camera model with the principal ray in the direction of the positive Z-axis.

C. Model

The deformable registration process is now described as a minimization of the energy function $\mathcal{E}$ with respect to the displacements φ of the vessel nodes in order to get the estimate φ' of φ, that is

$$\varphi' = \arg\min_{\varphi} \mathcal{E} \tag{1}$$

with the energy function

$$\mathcal{E} = D + \alpha S_L + \beta S_S \tag{2}$$

where the energy $\mathcal{E} : (G^3, G^2, C, \varphi) \mapsto y \in \mathbb{R}$ consists of a difference term $D : (G^3, G^2, C, \varphi) \mapsto y \in \mathbb{R}$ and regularization terms $S_L : (G^3, \varphi) \mapsto y \in \mathbb{R}$ for length preservation of the vessel segments, and $S_S : \varphi \mapsto y \in \mathbb{R}$ for smoothness of the displacement field. For brevity, we will drop the function arguments in the remainder of the paper. The positive scalars α and β control the influence of the respective terms.

In the following, we present the energy terms from (2). We also give the respective derivatives which are used in the gradient descent optimization scheme.

D. Difference Measure

The difference measure D which drives the registration process penalizes the distance between the projection of 3D points from the input graph and the corresponding 2D points from the input projection image.

Given point correspondences C with a single correspondence $C_i = (\mathbf{X}_i, \mathbf{x}_i)$ and a projection function $f : \mathbb{R}^3 \to \mathbb{R}^2$, we can define the distance measure

$$D = \frac{1}{n}\sum_{i=1}^{n} \left\| \mathbf{x}_i - f(\mathbf{X}_i + \varphi_i) \right\|^2 . \tag{3}$$

Here, $f : \mathbb{R}^3 \to \mathbb{R}^2$ is a projection function

$$f(\mathbf{X}) = \left(\mathbf{p}_1^\top \hat{\mathbf{X}} / \mathbf{p}_3^\top \hat{\mathbf{X}}, \mathbf{p}_2^\top \hat{\mathbf{X}} / \mathbf{p}_3^\top \hat{\mathbf{X}} \right)^\top \tag{4}$$

where $\mathbf{p}_1^\top$, $\mathbf{p}_2^\top$ and $\mathbf{p}_3^\top$ constitute the row vectors of the projection matrix $\mathbf{P} \in \mathbb{R}^{3\times 4}$, and $\hat{\mathbf{X}} = [\mathbf{X}^\top, 1]^\top$ is the homogeneous 4-vector representation of the 3D point $\mathbf{X}$.

For the minimization according to the model (2), the derivative of D with respect to φ_k is needed. By using $\mathbf{Y}_k = \mathbf{X}_k + \varphi_k$ the gradient is given by

$$\frac{\partial D}{\partial \varphi_k} = -\frac{2}{n} \left(\mathbf{x}_k - f(\mathbf{Y}_k) \right)^\top \mathbf{J}_k \tag{5}$$

where $\mathbf{J}_k \in \mathbb{R}^{2\times 3}$ is the Jacobian of f with respect to φ_k, given by

$$\mathbf{J}_k = \frac{1}{\left(\mathbf{p}_3^\top \hat{\mathbf{Y}}_k \right)^2} \times \begin{bmatrix} p_{11}\mathbf{p}_3^\top \hat{\mathbf{Y}}_k - p_{31}\mathbf{p}_1^\top \hat{\mathbf{Y}}_k & p_{21}\mathbf{p}_3^\top \hat{\mathbf{Y}}_k - p_{31}\mathbf{p}_2^\top \hat{\mathbf{Y}}_k \\ p_{12}\mathbf{p}_3^\top \hat{\mathbf{Y}}_k - p_{32}\mathbf{p}_1^\top \hat{\mathbf{Y}}_k & p_{22}\mathbf{p}_3^\top \hat{\mathbf{Y}}_k - p_{32}\mathbf{p}_2^\top \hat{\mathbf{Y}}_k \\ p_{13}\mathbf{p}_3^\top \hat{\mathbf{Y}}_k - p_{33}\mathbf{p}_1^\top \hat{\mathbf{Y}}_k & p_{23}\mathbf{p}_3^\top \hat{\mathbf{Y}}_k - p_{33}\mathbf{p}_2^\top \hat{\mathbf{Y}}_k \end{bmatrix}^\top \tag{6}$$

where p_{ij} denotes the entries of the projection matrix. For a detailed derivation of $\partial D / \partial \varphi_k$ please refer to the supplementary material.[4]

E. Length Preservation Constraint

Since vessel structures are in general enclosed by soft tissue, for example inside liver, and breathing motion is limited to a certain magnitude, the change of length of the vessels is limited. We model this observation by imposing a soft length preservation constraint on the single vessel segments. Thus, we do not impose constant lengths, which would be a too restrictive and unnatural assumption in the given setting. Since the vessel length is defined in 3D space, this constraint is able to induce a deformation orthogonal to projection rays, compare Fig. 4.

[3]In order to simplify the implementation, correspondences are computed only for sampling nodes, and thus also the energies are only evaluated there. This technical detail is due to the need to consider predecessor and successor nodes in some parts of the algorithm. Omitting the bifurcation nodes, which often have more than only two neighboring nodes, facilitates the implementation.

[4]http://campar.in.tum.de/personal/groher/tmi2d3ddeformable/groher2009tmi_suppMat.pdf

We define the terms $d_i^-(\varphi)$ and $d_i^+(\varphi)$, which measure the length of the edges connected to the sampling node $\mathbf{X}_i$ for a given set of displacements φ by

$$d_i^-(\varphi) = \|\mathbf{Y}_i - \mathbf{Y}_{i-1}\|^2 \tag{7}$$

and

$$d_i^+(\varphi) = \|\mathbf{Y}_i - \mathbf{Y}_{i+1}\|^2 \tag{8}$$

where we once again set $\mathbf{Y}_i = \mathbf{X}_i + \varphi_i$, compare also Fig. 6. The initial length of the edges connected to $\mathbf{X}_i$ is now given by $d_i^-(\mathbf{0})$ and $d_i^+(\mathbf{0})$ where $\mathbf{0}$ is the zero displacement field.

Now we can define a length preserving cost function as

$$S_L = \frac{1}{n}\sum_{i=1}^{n}\left|\frac{d_i^-(\mathbf{0}) - d_i^-(\varphi)}{d_i^-(\mathbf{0})}\right|^2 + \left|\frac{d_i^+(\mathbf{0}) - d_i^+(\varphi)}{d_i^+(\mathbf{0})}\right|^2 \tag{9}$$

which penalizes the relative deviation from the initial length of the two edges which are directly influenced by the i-th node.

The derivative of S_L with respect to φ_k reads

$$\frac{\partial S_L}{\partial \varphi_k} = \frac{-8}{n}\left[l_k^-(\mathbf{Y}_k - \mathbf{Y}_{k-1}) + l_k^+(\mathbf{Y}_k - \mathbf{Y}_{k+1})\right]^\top \tag{10}$$

with

$$l_k^- = \frac{d_k^-(\mathbf{0}) - d_k^-(\varphi)}{d_k^-(\mathbf{0})} \text{ and } l_k^+ = \frac{d_k^+(\mathbf{0}) - d_k^+(\varphi)}{d_k^+(\mathbf{0})}. \tag{11}$$

The evaluation of the derivative of the length preservation term is performed independently on single vessel segments Π, since for the computation, ordered correspondences and nodes with a left and right neighbor each are needed. Please, refer to the supplementary material[4] for a more detailed derivation of $\partial S_L/\partial \varphi_k$.

F. Diffusion Regularization

In order to impose a smoothness constraint onto the displacement field, we employ the regularization term S_S.

We implemented one of the common choices frequently used in intensity-based registration, the so-called diffusion regularization term (compare e.g., [4]). Any other standard regularization term, like bending energy, compare e.g., [29], can be used instead.

For defining the smoothing regularization energy, we employ the interpolating thin-plate spline model φ_{TPS} [26] to represent a continuous version of the displacement function, which is explicitly represented at the graph nodes by the vectors φ_i

$$\varphi_{\mathrm{TPS}}(\mathbf{X}) = \begin{bmatrix} \left(a_0^{(x_1)} + A^{(x_1)^\top}\mathbf{X} + \sum_{k=1}^n \omega_k^{(x_1)}\|\mathbf{X}_k - \mathbf{X}\|\right) - \mathbf{X}^{(x_1)} \\ \left(a_0^{(x_2)} + A^{(x_2)^\top}\mathbf{X} + \sum_{k=1}^n \omega_k^{(x_2)}\|\mathbf{X}_k - \mathbf{X}\|\right) - \mathbf{X}^{(x_2)} \\ \left(a_0^{(x_3)} + A^{(x_3)^\top}\mathbf{X} + \sum_{k=1}^n \omega_k^{(x_3)}\|\mathbf{X}_k - \mathbf{X}\|\right) - \mathbf{X}^{(x_3)} \end{bmatrix} \tag{12}$$

with $A^{(x_k)} = [a_1^{(x_k)}, a_2^{(x_k)}, a_3^{(x_k)}]^\top$, where the scalar values a_i and the vectors ω_k constitute the parameters of the TPS, which are computed to match the n given displacement values at the nodes of the graph, located at points $\mathbf{X}_k$.

The diffusion regularization cost function is then defined as

$$S_S = \frac{1}{n}\sum_{i=1}^{n}\left\|\nabla\varphi_{\mathrm{TPS}}^{(x_1)}(\mathbf{X}_i)\right\|^2 + \left\|\nabla\varphi_{\mathrm{TPS}}^{(x_2)}(\mathbf{X}_i)\right\|^2 + \left\|\nabla\varphi_{\mathrm{TPS}}^{(x_3)}(\mathbf{X}_i)\right\|^2. \tag{13}$$

The derivative of S_S is

$$\frac{\partial S_S}{\partial \varphi_k} = \frac{\partial S_S}{\partial \varphi_{\mathrm{TPS}}(\mathbf{X}_k)} \tag{14}$$

$$= -\frac{2}{n}\Delta\varphi_{\mathrm{TPS}}(\mathbf{X}_k) \tag{15}$$

$$= -\frac{2}{n}\left[\Delta\varphi_{\mathrm{TPS}}^{(x_1)}(\mathbf{X}_k), \Delta\varphi_{\mathrm{TPS}}^{(x_2)}(\mathbf{X}_k), \Delta\varphi_{\mathrm{TPS}}^{(x_3)}(\mathbf{X}_k)\right] \tag{16}$$

where the Laplace operator Δ with $\Delta\varphi_k^{(d)} = \partial_{x_1x_1}\varphi_k^{(d)} + \partial_{x_2x_2}\varphi_k^{(d)} + \partial_{x_3x_3}\varphi_k^{(d)}$ is evaluated analytically by computing $\Delta\varphi_{\mathrm{TPS}}^{(x_j)}(\mathbf{X})$ to

$$-\sum_{i=1}^{3}\sum_{k=1}^{n}\omega_k^{(x_j)}\left(\frac{-1}{\|\mathbf{X}_k - \mathbf{X}\|_\epsilon} + \frac{\left(\mathbf{X}_k^{(x_i)} - \mathbf{X}^{(x_i)}\right)^2}{\sqrt{(\mathbf{X}_k - \mathbf{X})^\top(\mathbf{X}_k - \mathbf{X}) + \epsilon}^3}\right). \tag{17}$$

The ϵ in the above equation is a small positive scalar, resulting from an approximation to the second norm $\|\mathbf{X}\|_\epsilon = \sqrt{\mathbf{X}^\top\mathbf{X} + \epsilon}$, in the TPS model from (12) in order to ensure its differentiability.

G. Optimization Scheme

By using all components of the cost function $\mathcal{E}$ together with their gradients, we can give an algorithm based on gradient descent optimization. Since our parameter space has a rather high dimension, the gradient descent optimization can get stuck in local minima. In order to avoid this, we incorporate a relaxation technique into our optimization. In an outer loop, the smoothness parameter β is gradually decreased while the inner part minimizes the energy with a given β in each iteration. The intuition behind this process is to impose a certain rigidity to the transformation if we are far away from the optimum, which is gradually relaxed the nearer we come to the global minimum in order to allow more local transformations. The relaxation process is controlled by a parameter T_{update}, which is usually set between 0.9 and 0.99. See Algorithm 1 for the pseudo code of our method.

As optimization method for Algorithm 1 we tested a steepest gradient descent as well as the Broyden–Fletcher–Goldfarb–Shanno (BFGS) optimizer [30]. The latter one brought a considerable speedup, which will be discussed in Section IV. For BFGS optimization we used the publicly available C++-routines of Jorge Nodecal.[5]

The values for the coefficients α and β are chosen empirically in the current implementation. For more details on parameter selection and definition of convergence criteria, please refer to Section III-A.

Fig. 7 shows an exemplary iteration process of the 2D-3D registration algorithm with steepest gradient descent optimization on a synthetic example. Note that the upper and lower part of the "C" shape are bent in the wrong direction after 85 iterations

[5]http://www.alglib.net/optimization/lbfgs.php.

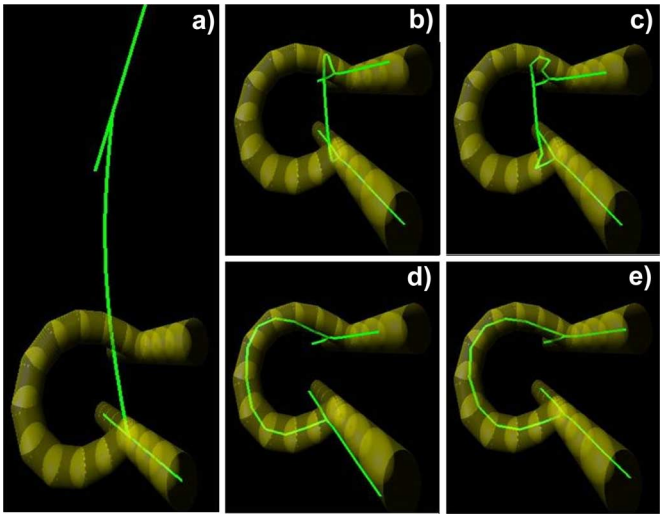

Fig. 7. Exemplary iteration process of the proposed 2D-3D deformable registration method with steepest gradient descent optimization. In each figure the yellow transparent surface represents the ground truth, the green line represents the centerline of the deformed 3D graph. The 2D graph to which the 3D graph is to be registered is not shown. The input setting is visualized in (a). The intermediate result is shown after 85 (b), 1012 (c), 3674 (d), and 7670 (e) iterations.

ALGORITHM 1

Algorithm 1 Deformable 2D-3D Registration with Additional Constraints

Given the input graphs G^3 and G^2, ordered point correspondences $C_i = (\mathbf{X}_i, \mathbf{x}_i)$, and a projection matrix $\mathbf{P}$,

initialize parameter T_{update}, β_{init}, β_{final}
$\beta \leftarrow \beta_{init}$
repeat
  //perform optimization
  repeat
    calculate $\nabla\mathcal{E} = \nabla D + \alpha\nabla S_L + \beta\nabla S_S$
    update displacements via a gradient descent step
    update the 3D TPS and deform whole graph
  until convergence
  //update β
  $\beta = T_{update} * \beta$
until $\beta < \beta_{final}$

[Fig. 7(c)], but the algorithm recovers from this situation as can be observed in Fig. 7(d) and (e).

H. Solving for 2D-3D Correspondences

We now extend our model to cope with a more general setup where corresponding information between 2D and 3D graph points is not known *a priori*.

There are many approaches to solve the correspondence problem while computing a transformation, possibly the most popular being the iterative closest point (ICP) [31], [32], which has been adapted and applied to medical data rather extensively [33]–[35]. We choose the model of Gold and Rangarajan [36], which is a *soft* version of the assignment as proposed by the ICP, and can be nicely integrated into our model.

Given a variable m_{ij}, where

$$m_{ij} = \begin{cases} 1, & \text{if } \mathbf{x}_i \text{ corresponds to } \mathbf{X}_j \\ 0, & \text{otherwise} \end{cases} \tag{18}$$

our energy can be extended to

$$\tilde{\mathcal{E}} = \tilde{D} + \alpha S_L + \beta S_S - \eta P \tag{19}$$

where the new difference term is defined as

$$\tilde{D} = \sum_{i=1}^{n}\sum_{j=1}^{N} m_{ij} \left\|\mathbf{x}_i - f(\mathbf{X}_j + \varphi_j)\right\|^2 \tag{20}$$

and a penalization term

$$P = \sum_{i=1}^{n}\sum_{j=1}^{N} m_{ij} \tag{21}$$

which avoids trivial solutions. Our optimization problem thus becomes

$$(\varphi', \mathbf{M}') = \arg\min_{\varphi,\mathbf{M}} \tilde{\mathcal{E}} \tag{22}$$

with additional parameters in the assignment matrix $\mathbf{M} = (m)_{ij}$.

In the standard ICP, m_{ij} is a binary variable, which can only take the values of 0 and 1. If this variable is directly put as a parameter into our optimization, many local minima arise and the optimization is likely to fail. Gold and Rangarajan proved that the transition of m_{ij} from a binary to a random variable $m_{ij} \in [0; 1]$, which takes the values

$$m_{ij} = \nu \exp \frac{-\|\mathbf{x}_i - \mathbf{x}_j\|^2}{2\nu} \tag{23}$$

will avoid the introduction of too many local minima [37].

To guarantee a 1-to-1 mapping, the assignment matrix $\mathbf{M}$ has to be doubly stochastic, i.e. the constraints $\sum_{i=1}^{n+1} m_{ij} = 1$ and $\sum_{j=1}^{N+1} m_{ij} = 1$ must be met, which can be approximated by row and column normalization [37].

Outliers are handled by introducing a *slack* row and column to ensure the constraints while being able to assign small probabilities to all entries of a row or column respectively that do not sum up to 1.

To further "convexify" the cost function, a deterministic annealing schedule is proposed, which renders the final energy

$$\tilde{\mathcal{E}} = \tilde{D} + \alpha S_L + \beta S_S - \eta P + \tau L \tag{24}$$

subject to the above constraints where, $L = \sum_{i=1}^{n}\sum_{j=1}^{N} m_{ij} \log m_{ij}$ is a so-called *entropy* term and τ the annealing parameter. The energy is minimized by an alternating scheme, where each iteration first applies the softassign given a transformation followed by an update of the transformation given correspondences [36]. An outer loop controls the annealing by gradually decreasing the annealing parameter τ.

This method of "softly" assigning correspondences combined with deterministic annealing has been successfully applied in

monodimensional rigid point-based registration [37], and has been extended to nonrigid registration as proposed by Chui and Rangarajan [38], who, to this end, introduce a TPS transformation model. Similar to our approach, they gradually decrease the smooting regularization parameter (β) according to the annealing scheme in order to allow for more local transformations if the algorithm approaches the global minimum.

I. Overall Algorithm

We adapt the update of correspondences to the projective case, yielding the final algorithm, which solves for both 2D-3D transformation and correspondences, see Algorithm 2. The parts, which have been taken from Algorithm 1 without change are held in light gray.

For criteria on convergence please refer to Section III-A. It should be emphasized that the row and column normalization includes the slack row and column to allow for outliers. Please note that the update of the assignment matrix takes the projection into account and thus evaluates the Euclidean distance in 2D. Moreover, the 2D correspondences used to compute the transformation are a mixture of all 2D points depending on their respective probabilities (compare [38]).

III. Results and Evaluation

In order to validate our results, besides visual inspection, we compute two different quantitative error measures.

The first measure is the 3D euclidean distance between the nodes of a given graph and the corresponding ground truth (GT) structure. We call this measure position error, which is given by

$$\frac{1}{n}\sum_{i=1}^{n}\left\|\mathbf{X}_i-\mathbf{X}_i^{GT}\right\| \tag{25}$$

where $\mathbf{X}_i$ are the positions of all nodes of a graph after registration, and $\mathbf{X}_i^{GT}$ are the positions of the corresponding nodes from the ground truth graph.

Since this first measure does not take topology into account we also introduce a second measure, which does not penalize the position, but only evaluates the shape. At every node, the angle between the two adjacent edges is computed. This measure is called the shape error, which is given by

$$\frac{1}{n-2}\sum_{i=2}^{n-1}\left|\arccos\frac{\mathbf{L}_i^{\top}\mathbf{R}_i}{\|\mathbf{L}_i\|\|\mathbf{R}_i\|}-\arccos\frac{\mathbf{L}_i^{GT\top}\mathbf{R}_i^{GT}}{\left\|\mathbf{L}_i^{GT}\right\|\left\|\mathbf{R}_i^{GT}\right\|}\right| \tag{26}$$

where $\mathbf{L}_i=\mathbf{X}_{i-1}-\mathbf{X}_i$, and $\mathbf{R}_i=\mathbf{X}_{i+1}-\mathbf{X}_i$. $\mathbf{L}_i^{GT}$, and $\mathbf{R}_i^{GT}$ are defined in an analogous manner. However, this error measure is suitable mostly for cases with a low number of nodes, since for large vessel systems, small random angle errors sum up to large values not describing the quality of the results in an appropriate manner.

We perform the tests on synthetic graphs with artificial deformations in order to test various aspects of the method. To demonstrate the applicability for real applications, we apply the tests to real vessels segmented from angiographic images, deformed by both, artificial and natural deformation fields. Moreover, we conduct a test on patient data coming from a clinical setting.

ALGORITHM 2

Algorithm 2 Deformable 2D-3D Registration with Unknown Correspondences

Given the input graphs G^3 and G^2, and a projection matrix $\mathbf{P}$,

initialize annealing parameters T_{init}, T_{update}, T_{final}, β_{final}
$\tau \leftarrow T_{init}$
$\varphi^{(0)} \leftarrow \mathbf{0}$
$\beta \leftarrow T_{init}\cdot\beta_{final}$
repeat
  //update assignment matrix according to Equation (23)
  $m_{ij}=\frac{1}{\tau}\exp\frac{-||\mathbf{x}_i-\mathbf{P}(\mathbf{X}_j+\varphi_j^{(t)})||^2}{2\tau}$
  repeat
    //row and column normalization
    $m_{ij}=\frac{m_{ij}}{\sum_{k=1}^{n+1}m_{kj}}\ ,\ \ j=1,\ldots,N$
    $m_{ij}=\frac{m_{ij}}{\sum_{k=1}^{N+1}m_{ik}}\ ,\ \ i=1,\ldots,n$
  until convergence
  //compute new correspondences
  if $\sum_{i=1}^{n}m_{ij}>thresh$ **then**
    $\mathbf{x}'_j=\sum_{i=1}^{n}m_{ij}\mathbf{x}_i\ ,\ \ j=1,\ldots,N$
  else
    discard point $\mathbf{X}_j$ as outlier
  end if
  //update the transformation on set $C_i=(\mathbf{X}_i,\mathbf{x}'_i)$, $i=1,\ldots,N$
  repeat
    calculate $\nabla\mathcal{E}=\nabla D+\alpha\nabla S_L+\beta\nabla S_S$
    update displacements via a gradient descent step
    update the 3D TPS and deform whole graph
  until convergence
  //update annealing parameter
  $\tau \leftarrow T_{update}*\tau$
  $\beta=T_{update}*\beta$
until $\tau<T_{final}$

A. Parameter Values

The parameter values used for the experiments were determined empirically. The value of $\alpha=0.01$, controlling the length preservation term, yields good results for all input data sets. For the smoothness term, $\beta_{\text{final}}=0.1$ was used as lower boundary of the relaxation scheme, i.e., the smoothness parameter was not allowed to drop below this value. The initial value for β at the beginning of relaxation was set to $\beta=T_{\text{init}}\cdot\beta_{\text{final}}$, as described in Algorithm 2. The parameter η is not set by the user, since the row and column constraints on the assignment matrix avoid trivial solutions automatically.

Annealing parameters are chosen such that the final value T_{final} is equal to the minimal distance between two nodes in 2D. T_{init} is set to $500\cdot T_{\text{final}}$ and the update parameter T_{update}, usually between 0.9 and 0.99, is set to 0.93.

The threshold for outlier removal (see Algorithm 2) is set to 0.01, i.e. if the sum of all probabilities in a column is below 1% this 3D point is assumed to have no corresponding 2D point.

TABLE I
RESULTS OF ERROR EVALUATION ON SEVERAL SYNTHETIC AND REAL DATA SETS WITH GIVEN CORRESPONDENCES. THE POSITION ERROR BY EUCLIDEAN DISTANCE, AS WELL AS THE SHAPE ERROR BY ANGLE MEASUREMENT IS ASSESSED. WE GIVE THE MEAN ERROR μ AND IN ORDER TO SHOW THE SIGNIFICANCE OF THE IMPROVEMENT ALSO THE STANDARD DEVIATION σ. FOR THE MEAN, THE RELATIVE IMPROVEMENT TO THE INPUT DATA IS GIVEN IN PERCENT. FOR VISUALIZATION OF THE SETTINGS, COMPARE FIGS. 8, 9, AND 11

Test Type		Position Error [mm]		Shape Error [rad]	
Test	**Data**	μ	σ	μ	σ
Synth 1	Input	4.46	3.58	0.5847	0.777
	Naïve	0.94 (78.9%)	1.06	0.4115 (29.6%)	0.514
	Result	0.87 (80.5%)	0.30	0.1459 (75.0%)	0.143
Synth 2	Input	1.36	1.09	0.3224	0.363
	Naïve	0.37 (72.8%)	0.47	0.2883 (10.58%)	0.307
	Result	0.17 (87.5%)	0.17	0.0780 (75.8%)	0.072
Synth 3	Input	1.42	0.80	0.3463	0.199
	Naïve	0.72 (49.3%)	0.57	0.2448 (29.3%)	0.174
	Result	0.84 (40.8%)	0.63	0.2218 (36.0%)	0.154
Liver 1	Input	7.38	2.23	0.1675	0.168
	Naïve	3.17 (57.0%)	2.85	0.1266 (24.4%)	0.127
	Result	3.70 (49.9%)	3.08	0.1428 (14.75%)	0.157
Liver 2	Input	1.20	0.65	0.0082	0.009
	Naïve	0.99 (17.5%)	0.68	0.0057 (30.5%)	0.008
	Result	0.99 (17.5%)	0.68	0.0062 (24.4%)	0.008
Liver 3	Input	14.88	15.0	0.2188	0.167
	Naïve	8.33 (44.0%)	4.53	0.2274 (-3.9%)	0.221
	Result	8.24 (44.6%)	5.17	0.2847 (-30.2%)	0.223

TABLE II
RESULTS OF ERROR EVALUATION ON SEVERAL SYNTHETIC AND REAL DATA SETS WITHOUT CORRESPONDENCES. THE POSITION ERROR BY EUCLIDEAN DISTANCE, AS WELL AS THE SHAPE ERROR BY ANGLE MEASUREMENT IS ASSESSED. WE GIVE THE MEAN ERROR μ AND IN ORDER TO SHOW THE SIGNIFICANCE OF THE IMPROVEMENT ALSO THE STANDARD DEVIATION σ. FOR THE MEAN, THE RELATIVE IMPROVEMENT TO THE INPUT DATA IS GIVEN IN PERCENT. FOR VISUALIZATION OF THE SETTINGS, COMPARE FIGS. 8, 9, AND 11

Test Type		Position Error [mm]		Shape Error [rad]	
Test	**Data**	μ	σ	μ	σ
Synth 1	Input	4.46	3.58	0.585	0.777
	Naïve	1.43 (67.74%)	0.94	1.261 (-116%)	1.129
	Result	0.81 (81.83%)	0.40	0.126 (78.4%)	0.135
Synth 2	Input	1.36	1.09	0.322	0.363
	Naïve	0.36 (75.3%)	0.47	0.288 (10.6%)	0.308
	Result	0.31 (77.2%)	0.07	0.023 (77.1%)	0.016
Synth 3	Input	1.42	0.80	0.346	0.199
	Naïve	1.21 (14.8%)	0.95	0.513 (-48.2%)	0.616
	Result	0.89 (37.5%)	0.67	0.271 (21.9%)	0.155
Liver 1	Input	7.38	2.23	0.168	0.168
	Naïve	7.84 (-6.2%)	6.43	0.754 (-350%)	0.636
	Result	3.44 (35.4%)	1.92	0.163 (2.69%)	0.163
Liver 2	Input	1.20	0.65	0.008	0.009
	Naïve	3.8 (-216%)	2.70	0.977 (<-500%)	0.701
	Result	1.15 (4.2%)	0.57	0.007 (9.76%)	0.009
Liver 3	Input	14.88	15.0	0.219	0.167
	Naïve	11.5 (22.7%)	6.40	0.283 (-29.3%)	0.208
	Result	10.71 (28.0%)	6.69	0.268 (-22.3%)	0.204

There are two inner loops listed in Algorithm 2, one for optimization, one for row and column normalization of the assignment matrix. Convergence for the optimization is tested by classical termination criteria, i.e., small parameter update, and small difference in energy values between successive iterations. The normalization loop is repeated 60 times, as suggested by Chui and Rangarajan [38].

B. Tests on Synthetic Data

For these tests, we use two 3D graphs, where one of the graphs is a deformed version of the other. The deformation is performed such that the length is not changed. To this end, we employ a dedicated deformation function, which is not used in our method itself, in order to assure the validness of comparison. The transformation is computed in the following way. Starting from an initial node, all remaining nodes are processed in a sequential manner. At every node, a rotation is performed about an axis passing through the previous node and being orthogonal to the plane formed by the Y-dimension and the projection ray. This ensures that most displacement happens along the projection rays, which gives an appropriate test setting for evaluating the role of the regularization terms. The rotation angle is varied at every node due to a trigonometric function, with a variable frequency and amplitude. The computed rotation is applied to the yet unprocessed part of the graph. Same applies also for the deformation used in Section III-C. The graph, which is not deformed serves as input for the method, while the deformed one presents the ground truth solution. The 3D ground truth is not directly used, but we generate a 2D projection of this structure, which is used as input for the method, together with the projection matrix. For three exemplary data sets (Synth1, Synth2, and Synth3) quantitative and visual results are presented in Tables I and II, and Fig. 11.

C. Real Data With Artificial Deformation

In order to assess the behavior of the method on natural vessel structures in a quantitative way, we deform the graphs extracted by segmentation from patient data sets with a length-preserving deformation function, as described in Section III-B. This way, we are able to perform our method and measure the distance of the result to a known ground truth in the same way as for synthetic data sets. A projection matrix computed from a rigid CTA-to-DSA registration of the respective patient is used to create the input 2D vessel graph. For the presented tests, we use a liver data set (Liver 1) from a patient who suffers from hepatocellular carcinoma and was treated with Transarterial Chemoembolization, compare Tables I and II and Fig. 8(a).

D. Real Data With Natural Deformation

Natural deformation fields for human organs are hard to obtain. In order to verify our method on possibly natural deformations we employ the results presented by Siebenthal *et al.* [39]. The displacement fields provided by this work are computed from a series of contrasted 4D MR images of the liver. A deformable registration is performed in [39] between the single 3D images, where the high time resolution together with the strong texture of the contrasted images assures the quality and reliability of the resulting deformation field. We segment the vessel structures from the contrasted MR images used in [39], and generate the input 3D graph for our method. Then, we apply the displacement field from [39] to the 3D graph and thus compute the ground truth for the result. A projection matrix yielding an anterior-posterior image was used for 2D input creation. In the same way as for the synthetic data sets, the 3D ground truth together with initial and deformed 3D input graph are used to quantitatively assess the performance of our method. Despite

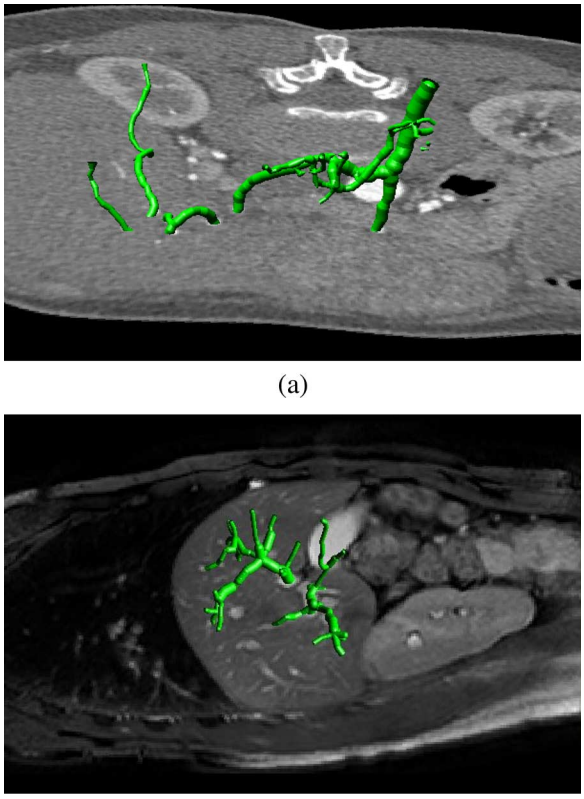

(a)

(b)

Fig. 8. Visualization of segmented real vessel structures. (a) Liver 1 data set (CTA) taken from a patient suffering from hepatocellular carcinoma. (b) Liver 2 data set (MRA) taken from Siebenthal *et al.* [39].

the small deformation observable in the data set (Liver 2), a clear improvement is achieved. Compare Tables I and II, and Fig. 8(b).

It can be observed that our method performs slightly better for the Liver 1 and 2 data sets if regularization is turned off and correspondences are known (compare Table I). This is due to the fact that for these data sets the deformation in ray direction is minor and regularization prevents the method to fully match in-plane deformation. Interestingly, however, the method performs better for all data sets if regularization is turned on and correspondences are not known (compare Table II). Our proposed regularization prevents the algorithm to assign false correspondences, which can happen easily when using the naïve method.

E. Test in a Clinical Setup

This test is performed with known projection matrices and a reference deformation field for comparison. An important issue for the creation of this reference deformation field is the correspondence problem on vascular 3D graphs, which we address in an intuitive manner by resampling and length accumulation in the first test and through careful manual inspection in the second and third tests.

For all tests we use two 3D graphs extracted from a preoperative CTA and an intraoperative cone-beam reconstruction of the same patient undergoing a liver catheterization. Both data sets have been acquired in deep inspiration. The intraoperative reconstruction is created from 395 views with projection matrices known from calibration. The 395 projections cover an angular range of 197° in 0.5° steps on a craniocaudal rotation axis.

First, we rigidly register the two 3D graphs. We manually determine point correspondences of all bifurcation points visible in both data sets. Unlike sampling nodes on vessel segments, the location of bifurcations is well-defined at the junction of a vessel graph and hence correspondency can be established. Then, we rigidly register the two resulting 3D point sets using the least-squares method of Umeyama [40].

1) Single Vessel Segment: Here, we test our algorithm in a simplified yet realistic environment by choosing only one vessel segment of the 3D vasculatures, which emanates from a bifurcation for which correspondency is known. We run our registration on this vessel segment only. Thus, we can automatically compute corresponding points using a length preserving constraint and hence reduce a possible bias in ground truth computation.

For computing a reference deformation field, we extract two vessel segments, $\Pi_{i,j}$ from the CTA graph and $\Pi'_{k,l}$ from the reconstruction graph that are manually determined to correspond. The chosen segment exhibits a large deformation, which is assessed after rigid 3D-3D registration of the complete vessel systems [see Fig. 9(a)]. We now want to establish correspondences between all sampling nodes of $\Pi_{i,j}$ and $\Pi'_{k,l}$ given the initial correspondences $\mathbf{B}_i \leftrightarrow \mathbf{B}'_k$.

The nodes on $\Pi_{i,j}$, $\Pi'_{k,l}$ cannot be assumed to have the same sampling since they have been extracted from two different data sets. Thus, we first apply a resampling to $\Pi'_{k,l}$ to have an internode distance which is significantly smaller compared to the internode distance of $\Pi_{i,j}$. Then, we assign correspondences to the sampling nodes in the following way: For a node $\mathbf{X} \in \Pi_{i,j}$ determine its curve length to $\mathbf{B}_i$, $d(\mathbf{B}_i, \mathbf{X})$. Walk through $\Pi'_{k,l}$ starting from $\mathbf{B}'_k$ until the first node $\mathbf{X}'$ has been found with $d(\mathbf{B}'_k, \mathbf{X}') \geq d(\mathbf{B}_i, \mathbf{X})$, which is assigned as corresponding node to $\mathbf{X}$. This procedure is repeated for all nodes in $\Pi_{i,j}$.[6]

With the set of correspondences $\{\mathbf{X}_h \leftrightarrow \mathbf{X}'_h\}$, $h = 1, \ldots, n_{i,j}$ we can compute a 3D Thin Plate Spline to align the two vessel segments $\Pi_{i,j}$ and $\Pi'_{k,l}$. The resulting spline is used to deform $\Pi_{i,j}$ to $\tilde{\Pi}_{i,j}$. With this method—in spite of the discretization error that is introduced—we observed the difference in length of $\Pi_{i,j}$ and $\tilde{\Pi}_{i,j}$ to be smaller than 6%.

As input for our registration method, we use the segment $\Pi_{i,j}$, the segment $\pi'_{k,l}$ which is the projection of $\Pi'_{k,l}$ by the matrix $\mathbf{P}_{\mathrm{rec}}$, and the correspondence information of the 3D segments. $\mathbf{P}_{\mathrm{rec}}$ is taken from one of the views used for reconstruction and thus resembles the 2D intraoperative situation, compare Fig. 9(b).

A considerable improvement in position and shape error can be observed when applying our algorithm, despite the large deformation of the vessel segment, compare the entries for Liver 3 in Table I.

A further test has been performed on this vessel segment with unknown correspondences using our extended Algorithm 2. The result is summarized in the entries for Liver 3 in Table II. It

[6]This sampling technique introduces an error to the assumption of length preservation, which is bounded by the inter-node distance of $\Pi'_{k,l}$.

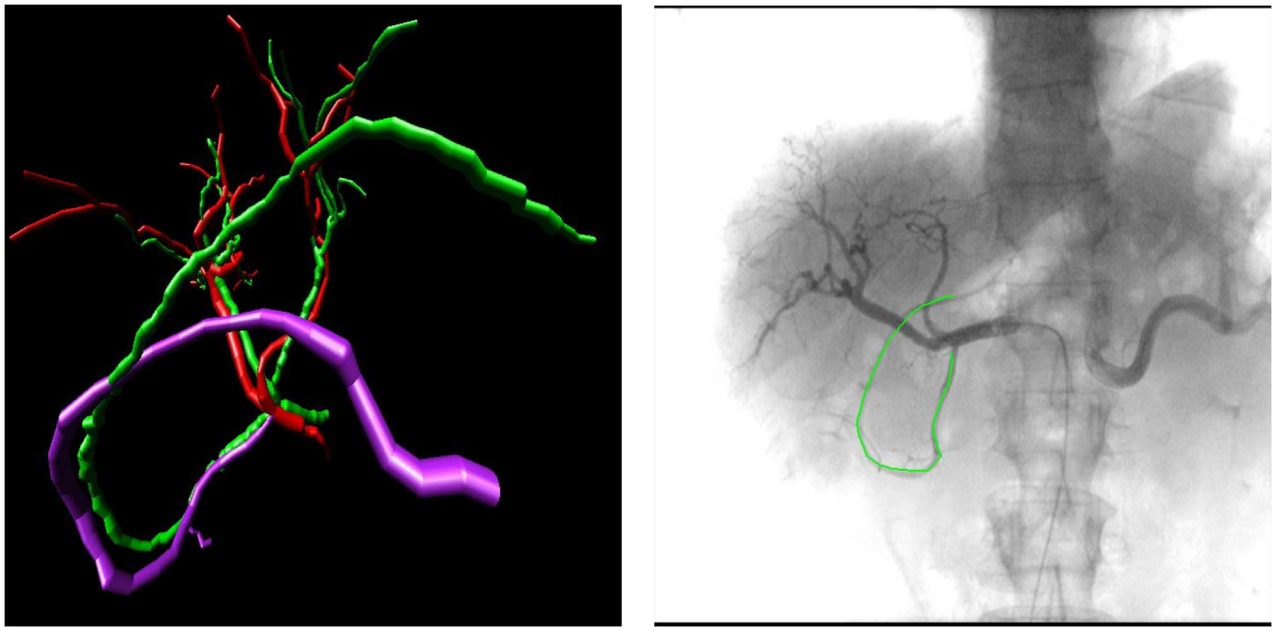

(a) (b)

Fig. 9. Clinical setup: (a) rigidly registered CTA (green) and intraoperative reconstruction (red and purple) of the vasculature. The purple vessel segment was used for the first clinical test. A large deformation is observable in this vessel compared to the corresponding, intersecting green vessel. (b) Projection of vessel segment onto an intraoperative 2D image. The 2D image was used for the intraoperative 3D reconstruction and a projection matrix is known due to calibration.

can be observed that the position error still improves more if regularization terms are incorporated. The shape error slightly increases, but again the impact of the regularization terms is shown when comparing to the naïve method.

Please note that the initial errors for the Liver 3 data set have been acquired after rigid registration.

2) Entire Vasculature Without Outliers: In this test, we deformed the entire vessel tree of the 3D reconstruction [red and purple vessels in Fig. 9(a)] to match the CTA vasculature [green vessels in Fig. 9(a)]. For that we manually identified 3D point correspondences and computed a 3D TPS. Then we registered this deformed vascular system "back" to 395 projections of the nondeformed vasculature using Algorithm 2. These projections were created using the vessel tree extracted from the original intraoperative reconstruction and the projection matrices with which it was computed. We use the graph extracted from original 3D reconstruction as ground truth to assess the position error.

Please note that, in order to be able to test the algorithm on a complex data set without outliers, we do not use the CTA vessel system as 3D input graph, but the intraoperative reconstruction, which is deformed to match the CTA vessel system. We conducted a test run, which computed 395 registrations. Moreover, we ran the test once more with both regularization terms set to zero. Both runs were performed with unknown correspondences.

Fig. 10(a) shows the position error of the 2×395 registrations. The horizontal line symbolizes the initial error. It can be observed that a naïve registration (without regularization) increases the error whereas our method benefits from the regularization terms to decrease the position error.

For images 180–210 and 260–280 the results are worse than neighboring results. These cases suffer from a heavy overlap of major vessels in the projections, which hampers the assignment of proper correspondences. This overlap is not present for the images where position errors are smaller after registration. However, in all cases, an improvement can be observed when comparing to the initial position error that was determined after rigid registration.

3) Entire Vasculature in the Presence of Outliers: This test is resembling the clinical scenario most realistically and adds the presence of outliers to the previous test. We used the vessel tree extracted from the preoperative CTA as 3D input. The 2D input graphs are created by projection of the 3D reconstruction that has been acquired intraoperatively. Again, the 395 projection matrices, which have been used in the previous test already, are taken to project the 3D reconstruction. The 3D reference deformation field for error assessment is computed by evaluating a 3D TPS on inverted correspondences used in the previous test.

It should be noted that the two data sets used for registration have been created from global and local injection of contrast agent and thus have a different level of propagation. Usually, dye propagates further down the vessel tree if injected locally through a catheter, which makes small vessels visible in the 3D reconstruction, which cannot be visualized in the CTA data set. Since the extraction of vessel graphs does not change vessel topology, there is a considerable amount of outliers in this test, compare Fig. 9.

As in the previous test, we computed 2×395 registrations using Algorithm 2, one run was conducted using our proposed model, one run with the naïve method, where smoothness and length preservation are excluded from the energy.

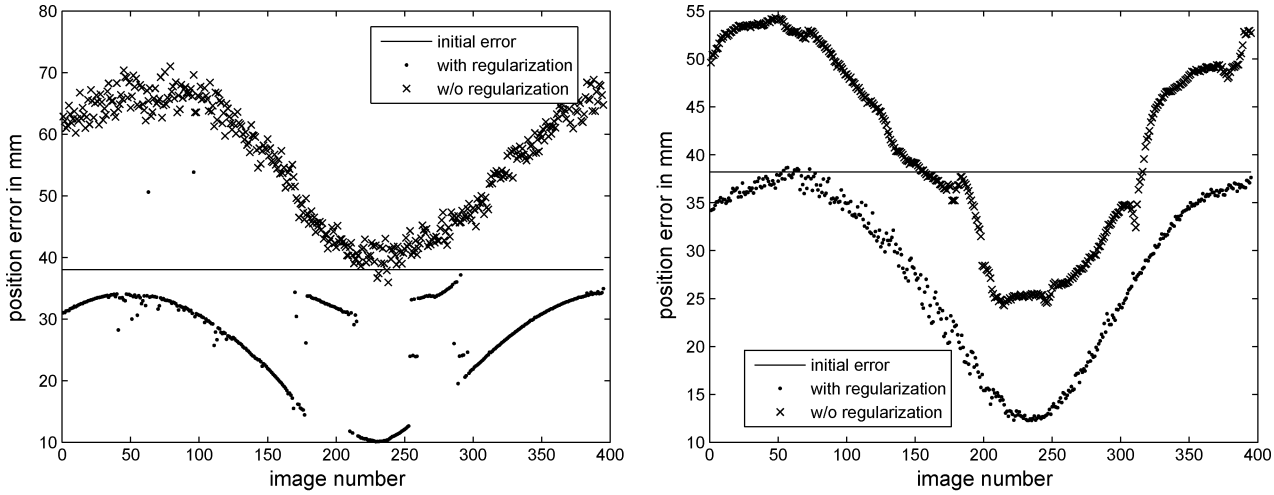

Fig. 10. Result of the two tests of (a) deformed 3D reconstruction (no outliers) and (b) with original CTA and 395 projections of the intraoperative 3D reconstruction (Sections III-E-2 and III-E-3). The dots show the error after registration with our algorithm, the crosses show the error after registration with the naïve method. The horizontal line symbolizes the initial error. It can be observed that a naïve registration increases the error whereas our method benefits from the regularization terms to decrease the position error.

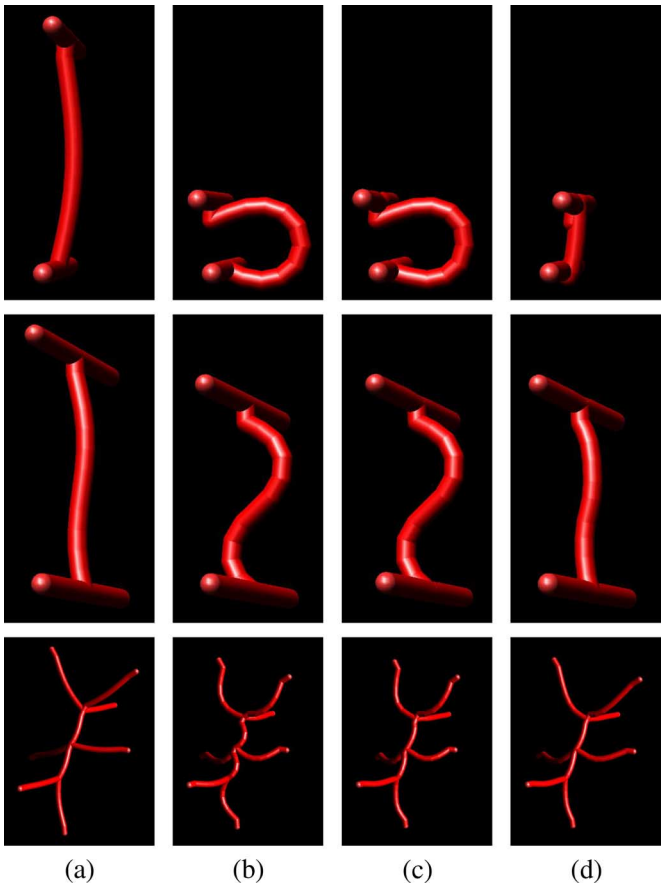

Fig. 11. Visualization of a selection of tests on synthetic data. Every row presents a single example setting, with the quantitative assessment of the results in Table I (from top to bottom: Synth 1, Synth 2, Synth 3). (a) 3D input. (b) Ground truth. (c) Our method (d) Naïve.

Fig. 10(b) shows the position error of the 2×395 registrations, again, the horizontal line shows the initial error (after rigid registration). As in the previous test, a considerable improvement can be observed when using our regularization techniques, whereas the naïve approach increases the error and cannot recover a correct solution.

In the 395 registrations that have been performed in the previous and the current section, the position error can be observed to increase in the first few registrations, decrease until half of the angular run is reached, and increase again until the end of the C-arm rotation. This penomenon can be explained with the geometric distribution of the liver vessel tree, which is mainly on the frontal plane. Thus, the first and last registrations, which use images of the anatomy from the left or right side of the patient, "compress" the geometric distribution of the vessel tree, which decreases the registration accuracy. However, even in these situtations our method can still find a solution, which decreases the position error compared to the initial rigid registration result.

IV. Discussion

In the previous section, we demonstrate that our method performs well in different scenarios. Even in the most general case where complex vascular systems are registered with unknown correspondences and in the presence of outliers, our experiments clearly reveal the impact and importance of our proposed regularization terms together with the difference term minimizing the euclidean error in 2D. We will now first briefly comment the clinical necessity of our proposed deformable registration method, followed by a discussion on the impact of the necessary previous steps on the accuracy, robustness and clinical feasibility. Moreover, runtime issues and possible ambiguities in the computed solution will be addressed.

A. Vessel Deformation in Clinical Routine

In clinical practice, pre- as well as intraoperative data sets are acquired in deep inspiration while the patient holds his breath. This will usually cause the vessel anatomy to be rather similar and only have a minimal amount of deformation. However, as

confirmed by our clinical partners, patients tend to hold their breath in different breathing states before and during the interventions. Moreover, inserted instruments like a guide wire or a catheter can also lead to vessel deformation. These issues can sometimes have a considerable effect on vessel deformation, which has also been shown in our clinical test setup, see Section III-E. Thus, we believe that 2D-3D deformable registration is crucial in this single-view angiographic scenario and will lead to more accurate results in terms of intraoperative navigation and guidance.

B. Segmentation

Our proposed method operates on 2D and 3D vessel features, which are extracted prior to the registration. The issue of using features rather than intensities for the registration influences our method in terms of accuracy and robustness.

Registration accuracy is directly dependent on the accuracy of the extracted vessel features. Since both, preoperative 3D data sets and intraoperative DSAs have a high intensity gradient (and thus intensity variation) at the vessel boundaries, even simple segmentation techniques like region growing yield results, which can be accurate up to a voxel/pixel precision. As state-of-the-art scanners can reconstruct volumes up to a submillimetric resolution, the metric segmentation error is rather small. In order to run our algorithm on the required features, we need to extract a centerline from the segmentation, which, in our experiments, employs topological thinning as described in [25]. This algorithm creates an approximation of a skeleton, which resembles the centerline in tubular structures. The approximation error is bounded by the radius of the vessel segments, which is below 2.5 mm for liver arteries. Assuming an error made by the skeletonization approximation of 1/4 of the radius, the propagated feature extraction error will be less than 0.625 mm corresponding to more than 1 voxel[7] in 3D and more than two pixels in 2D.[8] In summary, neither segmentation nor centerline extraction will introduce a large error. Region growing methods for vascular segmentation are usually very fast and involve a single seed point, which does not create much additional user interaction during an intervention. The process of topological thinning is fully automatic, rendering the feature extraction step feasible for clinical scenarios.

Due to different application of contrast agent in the two data sets (global injection in preoperative 3D data, local injection through a catheter in 2D data), our method has to deal with a certain amount of outliers (small vessel segments, which are only visible in 2D, segmented 3D vessel parts, which are not contrasted in 2D). This issue is addressed with the slack row/column in the assignment matrix (Section II-H), which makes the method more robust to outliers. Moreover, as can be depicted from the results in Fig. 10, length preservation and smoothness regularization penalize solutions where outliers contribute to the computed transformation.

Please note that the error evaluation is not affected by the segmentation error since the ground truth has always been computed from the 3D input vasculature using a deformation field.

[7]A typical voxel resolution in CTA data sets is $0.6 \times 0.6 \times 0.6\,\mathrm{mm}^3$.

[8]For a typical in-plane pixel resolution of $0.31 \times 0.31\,\mathrm{mm}^2$.

C. Rigid 2D-3D Registration

Our method can be carried out after a rigid 2D-3D registration has been performed since the model utilizes a previously computed projection matrix. Many catheterization interventions provide a preoperative data set from a CTA or MRA scan. In such a case, methods for rigid 2D-3D registration can be used to determine the projection matrix to an intraoperative 2D DSA [14]–[17].

Some hospitals use rotational angiography for acquisition of an intraoperative 3D data set. In this case, a projection matrix that projects the 3D data to match a currently acquired 2D DSA can be assembled from calibration data and table position of the imaging device [41].

Please note that our method is not solving for the entries of a projection matrix, but assumes them to be given in advance. Thus, inaccuracies of the estimated matrix directly affect the performance of our method. For intraoperative 3D data sets the estimated projection matrix is usually very accurate (in the range of submillimeters in the image plane) due to a precise offline calibration step [42], [43].

2D-3D registration methods for preoperative 3D data sets report in-plane errors below 5 mm and out-of-plane errors below 15 mm in a single-view scenario [14], [16], [17]. We have shown in the experiments that our method can cope with errors up to 3.8 cm, which makes a concatenation of rigid and deformable 2D-3D registration feasible.

D. Runtime

The runtime of our method depends on the number of graph nodes that are used in the optimization step. The 3D graphs used in the clinical evaluation in Section III-E have 160 and 320 nodes, respectively, which corresponds to a runtime of 3.2 and 4.3 min (averaged over the 395 registrations, executed single-threaded on a Intel Core 2 Duo 3 GHz). Together with 2D segmentation and rigid preregistration, this sums up to a runtime of ca. 5–7 min,[9] which is acceptable in an intraoperative situation as confirmed by our clinical partners.

E. Ambiguities

Our proposed method converges to the right solution in most cases. However, there are two special initial configurations where the energy function is not guaranteed to drive the gradient descent scheme to the correct solution. Both cases only occur if the deformation changes the sign in vessel curvature along the projection direction.

Typically, a gradient-based optimization algorithm will—given a suitable step size—converge to the "nearest" local optimum. Even if a vessel segment is deformed along the projection direction, the algorithm will compute the right deformation field given a suitable initial position. However, if the vessel segment either deforms from a straight line, or if it changes the sign of curvature during deformation, the proposed method is not guaranteed to converge to the right solution.

[9]Runtimes for segmentation and 2D-3D rigid registration have been taken from [17].

A segment, which is a straight line down to the precision of a single voxel is not very probable to be part of real vessel systems. Moreover, vessel systems are rather unlikely to invert their sign of curvature if they undergo a natural deformation due to e.g., patient breathing. Thus, we assume that these special cases do not occur frequently in real scenarios. Furthermore, if the curvature is computed for all vessel segments, straight lines can be detected, and the algorithm can indicate a possible convergence problem.

V. Concluding Remarks

In this paper, we present a method for deformable registration of 3D vessel structures to a single 2D projection image. We consider the 2D-3D pose estimation problem to be solved before the application of our method. We compute a 3D deformation field via the combination of a difference measure with constraints resulting from valid assumptions, and thus improve the rigid spatial alignment of the 3D vessel, which up to now presents the state of the art for this problem. Using the regularization terms S_L and S_S, we successfully account for the inherent ill-posedness of the problem, that is, the unknown deformation in projection direction. For estimating the correspondences between vessel feature points we choose a softassign method, which gradually determines the most probable correspondence between 2D and 3D locations. In an overall annealing schedule, both nonrigid transformation and correspondences are determined. The improvement in the spatial alignment is important for 3D depth perception and navigation during interventions. Furthermore, the physical plausibility of the results is increased due to the length preservation constraint. Quantitative and qualitative tests on clinical and synthetic data sets clearly demonstrate the improvement achieved by our method.

Acknowledgment

The authors would like to thank K. Klingenbeck-Regn, M. Pfister, Ali Khamene, and F. Sauer for their continuous support. We thank the Radiology Department of the Grosshadern Hospital, Munich, in particular M. Reiser, and T. Waggershauser for providing consistent data as well as insight into chemoembolization treatment. This paper is an extension of the paper "Deformable Registration of 3D Vessel Structures to a Single Projection Image" published in SPIE Medical Imaging 2008.

References

[1] S. Aylward and J. Jomier, "Rigid and deformable vasculature-to-image registration: A hierarchical approach," in *Proceedings of the International Conference Medical Image Computing and Computer Assisted Intervention (MICCAI)*. New York: Springer, 2004, vol. 3216, Lecture Notes Computer Science, pp. 829–836.

[2] A. Charnoz, V. Agnus, G. Malandain, C. Forest, M. Tajine, and L. Soler, "Liver registration for the follow-up of hepatic tumors," in *Proc. Int'l Conf. Medical Image Computing and Computer Assisted Intervention (MICCAI)*. New York: Springer, 2005, vol. 3750, Lecture Notes Computer Science, pp. 155–162.

[3] T. Rohlfing, C. R. Maurer, W. G. O'Dell, and J. Zhong, "Modeling liver motion and deformation during the respiratory cycle using intensity-based nonrigid registration of gated MR images," *Med. Phys.*, vol. 31, no. 3, pp. 427–432, 2004.

[4] J. Weickert and C. Schnörr, "A theoretical framework for convex regularizers in pde-based computation of image motion," *Int. J. Comput. Vis.*, vol. 45, no. 3, pp. 245–264, 2001.

[5] N. Alperin, D. N. Levin, and C. A. Pelizzari, "Retrospective registration of x-ray angiograms with MR images by using vessels as intrinsic landmarks," *J. Magn. Reson. Imag.*, vol. 4, pp. 139–144, 1994.

[6] J. Feldmar, N. Ayache, and F. Betting, "3D-2D projective registration of free-form curves and surfaces," in *Proc IEEE . Int. Conf. Comput. Vis.*, 1995, vol. 20–23, pp. 549–556.

[7] Y. Kita, D. Wilson, and J. Noble, "Real-time registration of 3D cerebral vessels to X-ray angiograms," in *Proceedings International Conference Medical Image Computing and Computer Assisted Intervention (MICCAI)*. New York: Springer, 1998, vol. 1496, pp. 1125–1133.

[8] A. Liu, E. Bullitt, and S. Pizer, "3D/2D registration via skeletal near projective invariance in tubular objects," in *Proceedings International Confernce Medical Image Computing and Computer Assisted Intervention (MICCAI)*. New York: Springer, 1998, vol. 1496, pp. 952–963.

[9] E. Kerrien, M.-O. Berger, E. Maurincomme, L. Launay, R. Vaillant, and L. Picard, "Fully automatic 3D/2D subtracted angiography registration," in *Proc. Int'l Conf. Medical Image Computing and Computer Assisted Intervention (MICCAI)*. New York: Springer, 1999, vol. 1679, Lecture Notes in Computer Science, pp. 664–671.

[10] A. C. S. Chung, I. William, M. Wells, A. Norbash, and W. E. L. Grimson, "Multi-modal image registration by minimising kull-back-leibler distance," in *Proc. Int'l Conf. Medical Image Computing and Computer Assisted Intervention (MICCAI)*. New York: Springer, Lecture Notes in Computer Science, pp. 525–532.

[11] J. Hipwell, G. Penney, R. McLaughlin, K. Rhode, P. Summers, T. Cox, J. Byrne, J. Noble, and D. Hawkes, "Intensity based 2D-3D registration of cerebral angiograms," *IEEE Trans. Med. Imag.*, vol. 22, no. 11, pp. 1417–1426, Nov. 2003.

[12] H. Chan, A. Chung, S. Yu, and W. Wells, "2D-3D vascular registration between digital subtraction angiographic (DSA) and magnetic resonance angiographic (MRA) images," in *Proc. IEEE Int. Symp. Biomed. Imag.*, 2004, vol. 1205, pp. 708–711.

[13] C. Florin, J. Williams, A. Khamene, and N. Paragios, "Registration of 3D angiographic and X-ray images using sequential Monte Carlo sampling," in *Computer Vision for Biomedical Image Applications, First Int'l Workshop, CVBIA* . New York: Springer, 2005, vol. 3765, Lecture Notes in Computer Science, pp. 427–436.

[14] G.-A. Turgeon, G. Lehmann, G. Guiraudon, M. Drangova, D. Holdsworth, and T. Peters, "2D-3D registration of coronary angiograms for cardiac procedure planning and guidance," *Med. Phys.*, vol. 32, pp. 3737–3749, 2005.

[15] M. Groher, T. Jakobs, N. Padoy, and N. Navab, "Planning and intraoperative visualization of liver catheterizations: New CTA protocol and 2D-3D registration method," *Academic Radiol.*, vol. 14, no. 11, pp. 1324–1339, 2007.

[16] J. Jomier, E. Bullitt, M. van Horn, C. Pathak, and S. Aylward, "3D/2D model-to-image registration applied to tips surgery," in *Proc. Int. Conf. Medical Image Comput. Computer Assisted Intervention (MICCAI)*, 2006, pp. 662–670.

[17] M. Groher, F. Bender, R. Hoffmann, and N. Navab, "Segmentation-driven 2D-3D registration for abdominal catheter interventions," in *Proc. Int. Conf. Med. Image Comput. Computer Assisted Intervention (MICCAI)*, 2007, vol. 4792, pp. 527–535.

[18] M. Fleute and S. Lavallee, "Nonrigid 3D/2D registration of images using statistical models," in *Proc. Int. Conf. Medical Image Computing Computer Assisted Intervention (MICCAI)*, 1999, pp. 138–147.

[19] S. Benameur, M. Mignotte, S. Parent, H. Labelle, W. Skalli, and J. de Guise, "3D/2D registration and segmentation of scoliotic vertebra using statistical models," *Computerized Medical Imaging Graphics*, vol. 27, pp. 321–337, 2003.

[20] J. Yao and R. Taylor, "Assessing accuracy factors in deformable 2D/3D medical image registration using a statistical pelvis model," in *Proc. Int. Conf. Computer Vis. (ICCV)*, Oct. 2003, vol. 2, p. 1329.

[21] G. Zheng, "A novel 3D/2D correspondence building method for anatomy-based registration," in *3rd Int'l. Workshop on Biomedical Image Registration*. New York: Springer, 2006, pp. 75–82.

[22] T. S. Y. Tang and R. E. Ellis, "2D/3D deformable registration using a hybrid atlas," in *Proc. Int'l Conf. Medical Image Computing and Computer Assisted Intervention (MICCAI)*. New York: Springer, 2005, vol. 3750, Lecture Notes in Computer Science, pp. 223–230.

[23] K. Grochow, S. L. Martin, A. Hertzmann, and Z. Popovic, "Style-based inverse kinematics," in *ACM Trans. Graphics*, 2004, vol. 23, no. 3, pp. 522–531.

[24] D. Selle, B. Preim, A. Schenk, and H.-O. Peitgen, "Analysis of vasculature for liver surgery planning," *IEEE Trans. Med. Imag.*, vol. 21, no. 11, pp. 1344–1357, Nov. 2002.

[25] K. Palágyi, E. Sorantin, E. Balogh, A. Kuba, C. Halmai, B. Erdöhelyi, and K. Hausegger, "A sequential 3D thinning algorithm and its medical applications," in *Proc. Int'l Conf. Information Processing in Medical Imaging*. New York: Springer, 2001, vol. 2028, Lecture Notes in Computer Science, pp. 409–415.

[26] G. Wahba, *Spline Models for Observational Data (C B M S-N S F Regional Conference Series in Applied Mathematics)*. Philadelphia, PA: SIAM, 1990.

[27] F. L. Bookstein, "Principal warps: Thin-plate splines and decomposition of deformations," *IEEE Trans. Pattern Anal. Mach. Intell.*, vol. 11, no. 6, pp. 567–585, Jun. 1989.

[28] K. Rohr, H. S. Stiehl, R. Sprengel, T. M. Buzug, J. Weese, and M. H. Kuhn, "Landmark-based elastic registration using approximating thin-plate splines," *IEEE Trans. Med. Imag.*, vol. 20, no. 6, pp. 526–534, Jun. 2001.

[29] D. Rueckert, L. Sonoda, C. Hayes, D. Hill, M. Leach, and D. Hawkes, "Nonrigid registration using free-form deformations: Application to breast MR images," *IEEE Trans. Med. Imag.*, vol. 18, no. 8, pp. 712–721, Aug. 1999.

[30] P. E. Gill, W. Murray, and M. H. Wright, *Practical Optimization*. New York: Elsevier, 1986.

[31] P. J. Besl and D. McKay, "A method for registration of 3D shapes," *IEEE Trans. Pattern Anal. Mach. Intell.*, vol. 14, no. 2, pp. 239–256, Feb. 1992.

[32] Z. Zhang, "Iterative point matching for registration of free-form curves and surfaces," *Int. J. Comput. Vis. (IJCV)*, vol. 13, pp. 119–152, 1994.

[33] G. Penney, P. Edwards, A. King, J. Blackall, P. Batchelor, and D. Hawkes, "A stochastic iterative closest point algorithm (stochastICP)," in *Proc. Int'l Conf. Medical Image Computing and Computer Assisted Intervention (MICCAI)*. New York: Springer, 2001, vol. 2208, pp. 762–769.

[34] S. Granger and X. Pennec, "Multi-scale EM-ICP: A fast and robust approach for surface registration," in *Proceedings of the 7th European Conference on Computer Vision-Part IV (ECCV'02)*. New York: Springer, 2002, pp. 418–432.

[35] R. S. J. Estepar, A. Brun, and C.-F. Westin, "Robust generalized total least squares iterative closest point registration," in *Proc. Int'l Conf. Medical Image Computing and Computer Assisted Intervention (MICCAI)*. New York: Springer, vol. 3216, Lecture Notes in Computer Science, pp. 234–241.

[36] S. Gold and A. Rangarajan, "A graduated assignment algorithm for graph matching," *IEEE Trans. Pattern Anal. Mach. Intell.*, vol. 18, no. 4, pp. 377–388, 1996.

[37] S. Gold, A. Rangarajan, C. Ping Lu, and E. Mjolsness, "New algorithms for 2D and 3D point matching: Pose estimation and correspondence," *Pattern Recognit.*, vol. 31, pp. 957–964, 1998.

[38] H. Chui and A. Rangarajan, "A new point matching algorithm for non-rigid registration," *Computer Vis. Image Understand.*, vol. 89, pp. 114–141, 2003.

[39] M. von Siebenthal, G. Székely, U. Gamper, P. Boesiger, A. Lomax, and P. Cattin, "4d MR imaging of respiratory organ motion and its variability," *Phys. Med. Biol.*, vol. 52, pp. 1547–1564, Feb. 2007.

[40] S. Umeyama, "Least-squares estimation of transformation parameters between two point patterns," *IEEE Trans. Pattern Anal. Mach. Intell.*, vol. 13, no. 4, pp. 376–380, 1991.

[41] S. Gorges, E. Kerrien, M.-O. Berger, Y. Trousset, J. Pescatore, R. Anxionnat, and L. Picard, "Model of a vascular C-Arm for 3D augmented fluoroscopy in interventional radiology," in *Proc. Int. Conf. Medical Image Computing Computer Assisted Intervention (MICCAI)*, 2005, pp. 214–222.

[42] N. Navab, A. Ben-Hashemi, M. M. Mitschke, D. W. Holdsworth, R. Fahrig, A. Fox, and R. Graumann, "Dynamic geometrical calibration for 3D cerebral angiography," *SPIE Med. Imag.*, pp. 361–370, 1996.

[43] H. Livyatan, Z. Yaniv, and L. Joskowicz, "Robust automatic C-Arm calibration for fluoroscopy-based navigation: A practical approach," in *Proc. Int. Conf. Medical Image Computing and Computer Assisted Intervention (MICCAI)*, 2002, vol. 2, pp. 60–68.

[44] D. Zikic, M. Groher, and N. Navab, "Deformable registration of 3D vessel structures to a single projection image," *SPIE Med. Imag.*, vol. 6914, p. 691412, Mar. 2008.